Modelling Simul. Mater. Sci. Eng. **18** (2010) 075003 (14pp) doi:10.1088/0965-0393/18/7/075003

Quantum mechanical study of solid solution effects on dislocation nucleation during nanoindentation

Qing Peng[1], Xu Zhang[1], Chen Huang[2], Emily A Carter[3] and Gang Lu[1]

[1] Department of Physics and Astronomy, California State University Northridge, Northridge, CA, USA
[2] Department of Physics, Princeton University, Princeton, NJ, USA
[3] Department of Mechanical and Aerospace Engineering and Program in Applied and Computational Mathematics, Princeton University, Princeton, NJ, USA

Received 22 June 2010
Published 24 August 2010
Online at stacks.iop.org/MSMSE/18/075003

Abstract

A multiscale quasicontinuum density functional theory method is used to study the solid solution effect on dislocation nucleation during nanoindentation. Specifically, an Al thin film with Mg impurities is considered. We find that the solid solution effect depends sensitively on the local configuration of the impurities. Although a random distribution of the impurities increases the hardness of the material, linear distributions of the impurities actually lower the hardness. In both cases, the strengthening/softening effects are due to dislocation nucleation. Consistent with recent experiments, the change of the ideal strength is found to be small. Different incipient plasticity behaviors are observed: in the pure material, two full dislocations are nucleated under the indentor. For a random distribution of impurities, two partial dislocations are formed instead. For linear distributions of impurities, only one partial dislocation is formed. Thus the nucleation of dislocations is sensitive to the local distribution of impurities in an alloy.

(Some figures in this article are in colour only in the electronic version)

1. Introduction

Solid solution strengthening, in which substitutional and/or interstitial impurities are introduced in materials, is a well-known strategy of improving mechanical strength of materials. Although the classical theory of solid solution strengthening [1] explains how impurities can increase the flow stress of bulk materials, the theory only accounts for dislocation propagation, not dislocation nucleation. In other words, the classical theory does not address whether dislocation nucleation plays an important role in the solid solution effects and to what extent impurities affect dislocation nucleation. The effect of dislocation nucleation on the mechanical strength of materials becomes particularly relevant and interesting in small scale mechanical testing such as in nanoindentation measurements, in contrast to large volume mechanical

testing that typically measures the motion of pre-existing dislocations under applied stresses. Nanoindentation, which evaluates the mechanical properties of small volumes of materials, can quantify the stress required to nucleate dislocations in dislocation-free solids [2–13]. In particular, the nanoindentation measurements can reach length scales modeled by atomistic methods, thus allowing direct comparisons with atomistic simulations.

Aluminum (Al) and Al alloys are widely used in both everyday life and in aerospace, packaging, construction, automotive and sports industries. Magnesium (Mg) is one of the most effective and commonly used alloying elements for aluminum. Al–Mg alloys possess many desirable physical properties, such as an advantageous strength to weight ratio, good fracture toughness and corrosion resistance that are superior to pure Al [14–16]. In the commercial Al–Mg alloys, Mg content ranges from 0.5% to 13%; while low-Mg Al alloys have the best formability, the high-Mg alloys often exhibit good castability and high strength.

Although the mechanism by which Mg impurities strengthen an Al alloy [17, 18] is well established, the same cannot be said for Mg's effect on dislocation nucleation in a dislocation-free or low-dislocation-density Al alloy. In particular, the relative importance of dislocation nucleation in the overall solid solution effects is not clear; the dependence of dislocation nucleation on the local configuration of the impurities is not well understood. As alluded to earlier, nanoindentation measurements are probably the best experimental approach to address these issues; they are capable of assessing elastic moduli and hardness of materials at small scales and exploring the elastic limit and incipient plasticity of crystalline solids [8, 10–12, 19]. Therefore, the capability to simulate the nanoindentation by realistic computer modeling could be very useful in both fundamental understanding of the solid solution effects on the ideal strength and perhaps design of alloys.

To study alloys with multiple elements, quantum mechanical simulations at large length scales are often desired. The reasons are two-fold. On one hand, quantum mechanical simulations are attractive because they are based on fundamental physical principles and do not depend on empirical input. By contrast, the simulations based on empirical potentials or force fields are reliable only in the regime in which the potentials were fit. In particular, fitting potentials for more than two elements has turned out to be exceedingly difficult. As a result, the transferability of empirical potentials is often questionable and their predictability for unknown structures and alloys is dubious at best.

In this paper, we use a multiscale approach whose energetics are determined *entirely* based on density functional theory (DFT). The method, termed QCDFT [20], combines the coarse gaining idea of the quasicontinuum (QC) approach and the coupling strategy of the quantum mechanics/molecular mechanics (QM/MM) method and represents an advance in the quantum simulation of materials properties. It should be stated, however, QCDFT is *not* a brute-force electronic structure method, but rather a multiscale approach that can treat large systems—effectively up to billions of electrons quantum mechanically. Therefore, some of the electronic degrees of freedom are reduced to continuum degrees of freedom in QCDFT. On the other hand, although QCDFT utilizes the idea of QM/MM coupling, it does not involve any classical/empirical potentials or force fields in the formulation—the energy calculation of QCDFT is entirely based on DFT.

Since QCDFT is formulated within the framework of the QC method, we shall give a short introduction to QC in section 2.1. In section 2.2, we briefly explain the local QCDFT calculation. In section 2.3, we summarize the DFT-based QM/MM approach that can treat the nonlocal QC region accurately and efficiently. In section 3, we apply QCDFT to study nanoindentation of an Al thin film in the presence and absence of Mg impurities. We present the nanoindentation results in section 4 and finally conclusions in section 5.

2. QCDFT methodology

2.1. QC method

The QCDFT method is an extension of the original QC method [21, 22] which models an atomistic system without explicitly treating every atom in the problem. In QC, the full set of N atoms is replaced with a small subset of N_{r} 'representative atoms' or *repatoms* ($N_{\mathrm{r}} \ll N$) that approximate the total energy through appropriate weighting. The repatoms are divided into two types, depending on their deformation state. Atoms experiencing large variations in the deformation gradient on an atomic scale are classified as *nonlocal* atoms and their energies are computed in the same way as in a standard atomistic method. In contrast, atoms experiencing a smooth deformation gradient field are classified as *local* atoms and their energies are computed based on the deformation gradient $\boldsymbol{G}$ in their vicinity. The total energy of the system is thus broken into two contributions:

$$\begin{aligned} E_{\mathrm{tot}}^{\mathrm{QCDFT}} &= E^{\mathrm{nl}} + E^{\mathrm{loc}} \\ &= E^{\mathrm{nl}}[\rho^{\mathrm{tot}}] + \sum_{j=1}^{N^{\mathrm{loc}}} n_j E_j^{\mathrm{loc}}(\{\boldsymbol{G}\}). \end{aligned} \tag{1}$$

Here ρ^{tot} is the total electron density of the system; n_j is the number of atoms that are represented by the jth repatom and E_j^{loc} is the energy density associated with the jth repatom. There are N^{loc} such local repatoms. The calculation in the nonlocal region is identical to that in first principles DFT methods whose energy depends on the electron density. On the other hand, the energy of a local repatom only depends on the deformation gradient $\boldsymbol{G}$ characterizing the finite strain around its position.

2.2. Local QC calculation with DFT

In the local QC region, a finite element mesh is constructed with each repatom on the vertices of surrounding finite elements. The energy and force of each local repatom can be obtained from the strain energy density and the stress tensor of the finite elements that share the same repatom. More specifically, according to the Cauchy–Born rule, the deformation gradient $\boldsymbol{G}$ is the same everywhere in a given finite element, therefore the local energy density and the stress tensor for each finite element can be calculated as a perfect infinite crystal undergoing a uniform deformation specified by $\boldsymbol{G}$.

For the deformation gradient $\boldsymbol{G_k}$ associated with the kth element, a periodic DFT calculation can be performed to determine the strain energy per unit cell $E^{\mathrm{DFT}}(\boldsymbol{G_k})$. The energy of the jth local repatom is a weighted sum of the strain energy $E^{\mathrm{DFT}}(\boldsymbol{G}_k)$ of the associated finite elements and expressed as

$$E_j^{\mathrm{loc}}(\{\boldsymbol{G}\}) = \sum_{k=1}^{M_j} w_{jk} E^{\mathrm{DFT}}(\boldsymbol{G}_k), \tag{2}$$

where M_j is the total number of finite elements shared by the jth repatom and w_{jk} is the weight associated with the kth finite element for the jth local repatom. The stress tensor of the kth element can be evaluated as follows:

$$\sigma_{ab} = \frac{1}{\Omega} \sum_{v} \frac{\partial E^{\mathrm{DFT}}(\boldsymbol{G}_k)}{\partial h_{av}} h_{bv} \tag{3}$$

with Ω being the volume of the deformed unit cell and h_{ij} denoting the ith Cartesian component of the deformed lattice vector h_j. The force on the jth local repatom is obtained from the stress

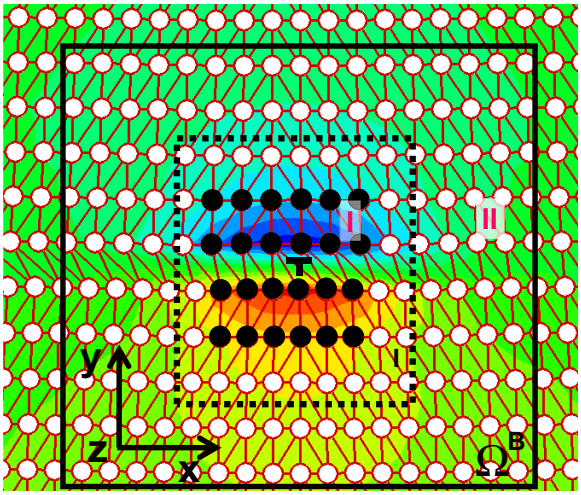

Figure 1. The schematic diagram of domain partitioning in QCDFT with a dislocation in an Al lattice as an example. The filled and open circles represent the nonlocal and buffer atoms, respectively. The dashed box represents Ω^{I} and the solid box represents the periodic box Ω^{B}. The volumes Ω^{I} and Ω^{B} are 2.8 Å and 8 Å beyond region I in the $\pm x$ and $\pm y$ directions, respectively.

tensor of surrounding finite elements [21]. The local QC formalism has been combined with orbital-free DFT (OFDFT) to predict dislocation nucleation in Al and Al_3Mg alloy [11, 12, 19].

2.3. Nonlocal QC calculation with DFT

For nonlocal QC calculations, a QM/MM approach is used. In a typical QM/MM calculation, the system is partitioned into two domains: a QM region and an MM region. In the context of QCDFT, the QM atoms refer to the nonlocal repatoms and the MM atoms refer to the buffer atoms which are a combination of both dummy atoms and local repatoms in QC terminology. The so-called dummy atoms, located in the local region, are not independent degrees of freedom, but rather slaves to the local repatoms. The position of a dummy atom is determined by the finite element interpolation from the relevant local repatom positions [21, 22]. The buffer atoms provide the appropriate boundary conditions for the nonlocal DFT calculation while the energy of the dummy atoms is still treated with the Cauchy–Born rule, consistent with their status. The self-consistent embedding theory [23–25] is employed for the QM/MM calculations. More specifically, both the energy of the nonlocal atoms and the interaction energy between the nonlocal atoms and the surrounding buffer atoms are calculated by DFT. To simply the notation, we denote the nonlocal region as region I, and the buffer region as region II, as shown in figure 1. Typically, the buffer region consists of several atomic layers surrounding the nonlocal region. We associate each buffer atom in region II with a valence electron density (ρ^{at}) and a pseudopotential; both of them are constructed *a priori* and remain fixed during a QM/MM simulation [24]. The nonlocal energy E^{nl} as defined in equation (1) can be expressed as

$$E^{\mathrm{nl}} = \min_{\rho^{\mathrm{I}}}\{E_{\mathrm{DFT}}[\rho^{\mathrm{I}}; \boldsymbol{R}^{\mathrm{I}}] + E^{\mathrm{int}}_{\mathrm{OF}}[\rho^{\mathrm{I}}, \rho^{\mathrm{II}}; \boldsymbol{R}^{\mathrm{I}}, \boldsymbol{R}^{\mathrm{II}}]\}. \tag{4}$$

Here $\boldsymbol{R}^{\mathrm{I}}$ and $\boldsymbol{R}^{\mathrm{II}}$ denote atomic coordinates in region I and II, respectively. The charge density of region I, ρ^{I}, is the degree of freedom and is determined self-consistently by minimizing the nonlocal energy functional. The charge density of region II, ρ^{II}, is defined as the superposition

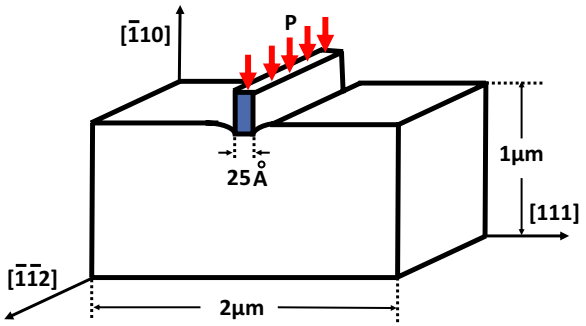

Figure 2. Schematic representation of the nanoindentation of Al thin film showing the relevant dimensions and orientations.

of atomic-centered charge densities ρ^{at}, which only changes upon the relaxation of region II ions. The interaction energy, $E_{\mathrm{OF}}^{\mathrm{int}}$, formulated by OFDFT [26, 27] is defined as follows:

$$E_{\mathrm{OF}}^{\mathrm{int}}[\rho^{\mathrm{I}}, \rho^{\mathrm{II}}; \boldsymbol{R}^{\mathrm{I}}, \boldsymbol{R}^{\mathrm{II}}] = E_{\mathrm{OF}}[\rho^{\mathrm{tot}}; \boldsymbol{R}^{\mathrm{tot}}] - E_{\mathrm{OF}}[\rho^{\mathrm{I}}; \boldsymbol{R}^{\mathrm{I}}] - E_{\mathrm{OF}}[\rho^{\mathrm{II}}; \boldsymbol{R}^{\mathrm{II}}], \tag{5}$$

where $\boldsymbol{R}^{\mathrm{tot}} \equiv \boldsymbol{R}^{\mathrm{I}} \bigcup \boldsymbol{R}^{\mathrm{II}}$ and $\rho^{\mathrm{tot}} = \rho^{\mathrm{I}} + \rho^{\mathrm{II}}$. A single-particle embedding potential $\mu_{\mathrm{emb}}(\boldsymbol{r})$ can be defined as a functional derivative of the interaction energy with respect to ρ^{I}

$$\mu_{\mathrm{emb}}(\boldsymbol{r}) \equiv \frac{\delta E_{\mathrm{OF}}^{\mathrm{int}}[\rho^{\mathrm{I}}, \rho^{\mathrm{II}}; \boldsymbol{R}^{\mathrm{I}}, \boldsymbol{R}^{\mathrm{II}}]}{\delta \rho^{\mathrm{I}}}, \tag{6}$$

which represents the effective potential that region I electrons feel due to the presence of region II [23, 24]; it is through $\mu_{\mathrm{emb}}(\boldsymbol{r})$ that the QM/MM coupling is achieved quantum mechanically at the level of OFDFT. The embedding potential provides boundary conditions for ρ^{I} and is updated self-consistently during the minimization of the nonlocal energy functional. A basic ansatz of the nonlocal energy functional (equation (4)) is that ρ^{I} must be confined within a finite volume (Ω^{I}) that is necessarily *larger* than region I, as shown in figure 1. In other words, ρ^{I} vanishes beyond Ω^{I}. In addition, to efficiently compute some terms in the formulation of equation (5) using fast Fourier transform, we also introduce a volume Ω^{B} (as shown in figure 1) over which the periodic boundary conditions are applied. The details of implementation of the periodic boundary conditions can be found in [24].

3. Computational details

3.1. Model setup

The present QCDFT approach is applied to simulate the nanoindentation of an Al thin film resting on a rigid substrate below a rigid knife-like indenter. We choose this particular system because there exists a good kinetic energy functional (required for OFDFT calculations) and EAM potential [28] for Al. In this paper, we have rescaled the 'force-matching' EAM potential of Al [28] so that it matches precisely the DFT value of the lattice constant and bulk modulus of Al [20].

The crystallographic orientation of the system is displayed in figure 2. The size of the entire system is 2 μm × 1 μm × 4.9385 Å along the [1 1 1] (x direction), the [$\bar{1}$ 1 0] (y direction) and the [$\bar{1}$ $\bar{1}$ 2] (z direction), respectively. The system is periodic in the z-dimension and has Dirichlet boundary conditions in the other two directions. The entire system contains over 60 million Al atoms—a size that is beyond the reach of a full-blown quantum mechanical

calculation in which all atoms are treated explicitly. The unloaded system is a perfect single crystal similar to a typical experimental situation. The film is oriented so that the preferred slip system $\langle 1\,1\,0\rangle\{1\,1\,1\}$ is parallel to the indentation direction to facilitate dislocation nucleation. The indenter is a rigid flat indenter of width 25 Å. We assume the perfect-stick boundary condition for the indenter so that the Al atoms in contact with it are not allowed to slip. The knife-like geometry of the indenter is dictated by the pseudo-two-dimensional (2D) nature of the QC model adopted here. Three-dimensional QC models do exist and can be implemented in QCDFT [11, 12, 29]. We choose to work with the pseudo-2D model in this example for simplicity. The prefix *pseudo* is meant to emphasize that although the analysis is carried out in a 2D coordinate system, out-of-plane displacements are allowed and all atomistic calculations are three-dimensional. Within this setting, however, only dislocations with line directions perpendicular to the xy plane can be nucleated.

The simulation is performed quasistatically with a displacement control where the indentation depth (d) is increased by 0.1 Å at each loading step. Because DFT calculations are much more expensive than EAM, we use EAM-based QC [8] to relax the system for most of the loading steps at first. At $d = 2.0, 3.0, 5.5, 6.0, 7.0, 7.1, 7.5$ Å, the corresponding EAM configurations are further relaxed by QCDFT. The QCDFT loadings are carried out after $d = 7.5$ Å starting from the full relaxed EAM-QC configuration of previous loading step, until the onset of the plasticity occurs at $d = 8.2$ Å for pure Al.

To study the effect of Mg impurities on the ideal strength and incipient plasticity of the Al thin film, three different cases are considered, each with five Mg impurities. Since the simulations are quasi-2D and the periodic boundary condition is applied along the $[\bar{1}\,\bar{1}\,2]$ direction, we are effectively simulating a row of Mg impurities interacting with (nucleated) straight dislocations. Therefore, although the apparent concentration of Mg impurities in the simulations is about 0.1 ppm, the concentration of Mg impurities along the $[\bar{1}\,\bar{1}\,2]$ is very high (the neighboring Mg impurities are separated by ∼5 Å). These five Mg impurities are placed in three different geometries: (i) randomly below the indenter, as schematically shown in figure 3(*b*), referred to as *random*; (ii) a linear configuration on the tension side of the slip plane, as schematically shown in figure 3(*c*), referred to as *tension*. In this case, the impurities are placed below the slip plane of a nucleated edge dislocation whose extra atomic plane is above the slip plane. (iii) A linear configuration on the compression side of the slip plane as schematically shown in figure 3(*d*), referred to as *compression*. In this case, the impurities are on the same side of the extra atomic plane of the dislocation. The reference system of pure Al is referred to as *pure*. In the following QCDFT calculations, the pure system is relaxed first, then the impurities are introduced followed by full relaxation again.

The parameters of the OFDFT kinetic energy functional with a density-dependent kernel are from [27]. Since OFDFT is an approximation to Kohn–Sham DFT (KSDFT), fitting parameters to a more exact KSDFT theory keeps the method fully non-empirical, which is very important. The local pseudopotential for Al and Mg ion is taken from [30, 31], respectively. The local-density approximation (LDA) [32] is used for the exchange-correlation functional. A high kinetic energy cutoff for the plane wave basis of 1600 eV is used to ensure the convergence of the charge density. Nonlocal interactions are included in OFDFT, through the nonlocal Coulomb interaction and the nonlocal kinetic energy density functional. For the nonlocal calculation, the grid density in volume Ω^{I} is 5 grid-points per Å. The Ω^{I} box goes beyond the nonlocal region by 2.8 Å in the $\pm x$ and $\pm y$ directions so that ρ^{I} decays to zero at the boundary of Ω^{I}, as shown in figure 1. The periodic box Ω^{B} extends 8.0 Å in the $\pm x$ and $\pm y$ directions beyond the nonlocal region. The relaxation of all repatoms is performed by the conjugate gradient method until the maximum force on any repatom is less than 0.03 eV Å^{-1}. The typical dimensions of a nonlocal QCDFT calculation are $60 \times 60 \times 4.9385$ Å^3, containing

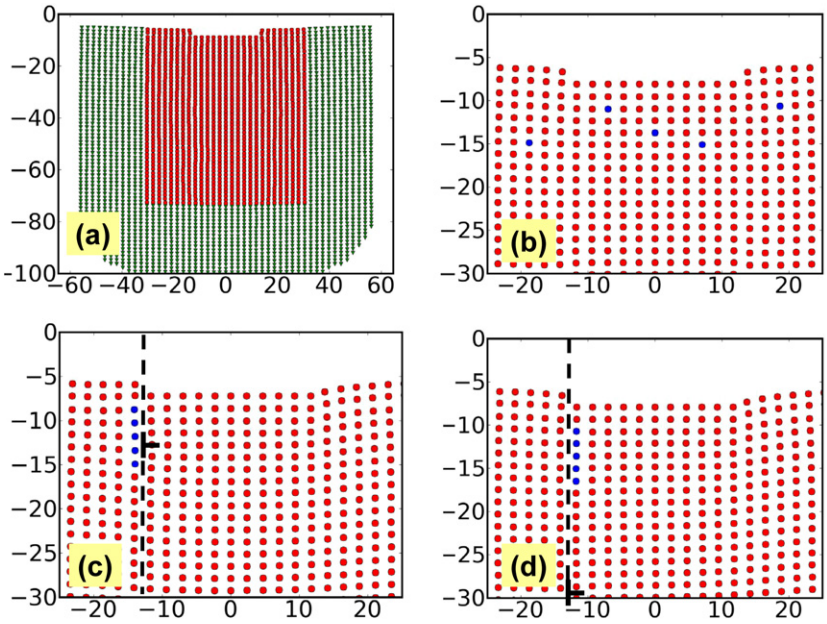

Figure 3. Schematic diagram of Mg impurities in the Al thin film corresponding to (a) *pure*, (b) *random*, (c) *tension*, (d) *compression* cases. The red/light grey and blue/dark grey circles represent nonlocal Al and Mg atoms, respectively. The dashed line indicates the active slip plane for the nucleated dislocations. The axis units are given in Å.

approximately 1300 nonlocal atoms and 2000 dummy atoms. There are correspondingly 3200 finite elements in the local region. Overall, the system effectively contains over 60 million atoms. The standard QC procedure for re-meshing is used in the calculations. Taking the eigenvalues of the deformation gradients in two neighboring finite elements a and b to be λ_k^a and λ_k^b ($k = 1, 2, 3$), the nonlocality (or re-meshing) is triggered if $\max_{a,b;k}|\lambda_k^a - \lambda_k^b| > \delta$, where δ is the nonlocality criterion [21]. In this paper, δ is taken as 0.15.

At $d = 3.0, 6.0, 7.5$ Å, the full QCDFT relaxations are performed for the pure system first, then the random distribution of impurities is introduced, followed by full QCDFT relaxations again. The QCDFT calculations are carried out after $d = 7.5$ Å starting from the fully relaxed configuration of the previous loading step, until the onset of the plasticity occurs at $d = 8.1$ Å. At $d = 3.0, 5.5, 6.0, 7.0$ Å, the *tension* results are obtained after full QCDFT relaxations of the *pure* Al system. The QCDFT calculations are performed after $d = 7.0$ Å starting from the fully relaxed configuration of the previous loading step, until the onset of the plasticity occurs at $d = 7.2$ Å. At $d = 3.0, 5.5, 6.0, 7.0, 7.5$ Å, the *compression* results are obtained after full QCDFT relaxations of the *pure* Al system. The QCDFT calculations are carried out after $d = 7.5$ Å starting from the fully relaxed configuration of the previous loading step, until the onset of the plasticity occurs at $d = 7.9$ Å.

3.2. Elastic moduli

To put the nanoindentation results in context, we first calculate the elastic moduli of bulk Al using the periodic OFDFT method. The fcc crystal has three independent elastic constants C_{11}, C_{12} and C_{44}. As a result, a set of three equations is need to determine the elastic constants and moduli. Three highly symmetrical modes of deformation are applied in the OFDFT

Table 1. Elastic constants, moduli and Poisson's ratio obtained by OFDFT on bulk Al for pure Al and two concentrations of Mg impurities.

	Pure	0.2%	1%
C_{11} (GPa)	88.22	88.32	87.80
C_{12} (GPa)	55.84	55.87	55.25
C_{44} (GPa)	30.11	30.20	30.95
K (GPa)	66.63	66.69	66.10
μ (GPa)	24.55	24.61	25.08
ν	0.3360	0.3357	0.3316

calculations. The cubic computational supercell ($5 \times 5 \times 5$) contains 500 Al atoms for the pure system, 499 Al atoms and 1 Mg atom for the 0.2% impurity system and 495 Al atoms and 5 Mg atoms which are arranged randomly for 1% impurity system, respectively. Periodic boundary conditions are applied in all three directions. The computational parameters of the stand-alone OFDFT calculations are the same as those used in the QCDFT calculations. The total energy is calculated as a function of applied strain to the supercell, from which the elastic moduli and constants are determined. The goal of the calculations is to estimate the effect of the impurity on the elastic moduli and constants. The first applied deformation mode is equiaxial, for calculating the bulk modulus K, which is related to the elastic constants by $K = \frac{1}{3}(C_{11} + 2C_{12})$. The second mode of deformation is the volume-conserved tetragonal strain. The strain tensor is given as $\begin{pmatrix} \epsilon & 0 & 0 \\ 0 & \epsilon & 0 \\ 0 & 0 & \frac{1}{(1+\epsilon)^2} - 1 \end{pmatrix}$, where $\epsilon = (1 + e)^{-1/3} - 1$. Here e is related to the lattice constant ratio c/a by $c/a = 1 + e$. The third mode of deformation is a rhombohedral distortion, with the strain tensor $\frac{e}{3}\begin{pmatrix} 1 & 1 & 1 \\ 1 & 1 & 1 \\ 1 & 1 & 1 \end{pmatrix}$. C_{11}, C_{12}, C_{44} can be obtained through the previous three deformation modes [33, 34]. The shear modulus μ and Poisson's ratio ν are computed from the elastic moduli by a Voigt average [35]: $\mu = (C_{11} - C_{12} + 3C_{44})/5$ and $\nu = (C_{11} + 4C_{12} - 2C_{44})/(2(2C_{11} + 3C_{12} + C_{44}))$. The results are summarized in table 1. The elastic constants except C_{44} seem to have a complicated dependence on Mg concentration. On the other hand, the shear modulus μ and C_{44} appear to increase as a function of Mg concentration. However, for the concentrations considered here, the increase in the shear modulus is modest, about 2%.

3.3. Generalized stacking fault energy (GSFE)

We also calculated the (1 1 1) plane GSFE along the $[\bar{1}\ 1\ 0]$ and $[\bar{1}\ \bar{1}\ 2]$ directions in the presence and absence of Mg impurities. GSFEs in both directions are relevant because dislocations in fcc metals tend to dissociate into Shockley partial dislocations that acquire displacement vectors in both directions. We carried out three calculations to examine the dependence of the GSFE on the concentration of the impurities. More specifically, three supercells are constructed, which contain 24, 60 and 600 atoms, respectively, distributing equally into six layers. In the layer adjacent to the stacking fault, 1 Mg impurity is introduced in the first and the second supercell and 5 Mg impurities are introduced in the third supercell, corresponding to an overall Mg concentration of 4.17%, 1.67% and 0.83%, respectively. In the case of 5 Mg impurities, Mg atoms are arranged both randomly and linearly. The linear distribution of the impurities is along the $[\bar{1}\ 1\ 0]$ direction, corresponding to the QCDFT configuration. The intrinsic stacking fault (ISF) energy for both impurity distributions is given in table 2. Note that the ISF energy for the linear distribution of the impurities is listed under the column of compression/tension for convenience.

Table 2. The shear modulus μ, ISF energy $\gamma_{\rm isf}$, stacking fault width w measured from QCDFT calculation results and the dislocation energy $E^{\rm dis}$ (calculated with equation (7)), corresponding to the *pure*, *random*, *compression* and *tension* cases.

	Pure	Random	Compression	Tension
μ (GPa)	24.55	25.08	25.07	25.07
$\gamma_{\rm isf}$ (J m^{-2})	0.12	0.11	0.11	
w (Å)	20,20	32,30	28	7
$E^{\rm dis}$ (eV)	3.94	3.03	1.37	0.67

The computational details of GSFE surface can be found from [36, 37]. The atomic relaxation along the direction that is perpendicular to the slip plane is found to be small. For example, the lattice vectors of the 600-atom supercell are given by $\begin{pmatrix} 2\sqrt{3} & 0 & 0 \\ 0 & 25\sqrt{2} & 0 \\ 0 & 0 & \frac{\sqrt{6}}{2} \end{pmatrix} a_0$. Here a_0 is the equilibrium lattice constant. The results for GSFEs of different concentrations of impurities are plotted in figure 4. Because of the reflection symmetry along $[\bar{1}\,1\,0]$, only one-half of the GSFE curve is shown in the left column of figure 4. Along the $[\bar{1}\,\bar{1}\,2]$ direction, only the relevant portion of the GSFE, which includes the displacement up to the ISF, is shown. The general trend is an increasing change in the GSFE with increasing Mg content. At a low concentration of 0.83%, the increase in GSFE is negligible. Interestingly, the ISF energy (the end-point in the $[\bar{1}\,\bar{1}\,2]$ direction) of the alloys is actually slightly reduced compared with the pure system for all three concentrations considered here. For a comparison purpose, we have also calculated the $(1\,1\,0)$ surface energy $\gamma_{1\,1\,0}$, using the embedding-atom-method (EAM), OFDFT and KSDFT methods, respectively; the numbers are $\gamma_{1\,1\,0} = 0.93\,{\rm J\,m^{-2}}$ (EAM), $1.05\,{\rm J\,m^{-2}}$ (OFDFT) and $0.99\,{\rm J\,m^{-2}}$ (KSDFT) J m^{-2} respectively. They are much larger than the GSFEs.

4. Results and discussion

The load–displacement curve is the typical observable for nanoindentation, and is widely used both experimentally and theoretically, often serving as a link between the two. In particular, it is conventional to identify the onset of incipient plasticity with the first drop in the load–displacement curve during indentation [7–11, 13, 20, 29, 38, 39]. In this work, the load is given in N m^{-1}, normalized by the length of the indenter in the out-of-plane direction.

For pure Al, the load–displacement (P–d) curve shows a linear relation initially, followed by a drop at $d = 8.2$ Å in figure 5. The drop corresponds to the nucleation of dislocations beneath the indenter—the onset of plasticity. A pair of edge dislocations are nucleated at $x = \pm 13$ Å, and $y = -45$ Å. In figure 6, we present the out-of-plane (or screw) displacement u_z of the nonlocal repatoms. The non-zero screw displacement of the edge dislocations suggests that each dislocation is dissociated into two $1/6\langle 1\,1\,2\rangle$ Shockley partials bound by a stacking fault with a width of about 20 Å. The activated slip planes are $\{1\,1\,1\}$ type and are adjacent to the edges of the indenter. The slope for the linear part of the curve is 27.1 GPa, which is greater than the shear modulus $\mu = 24.6$ GPa but less than $C_{44} = 30.1$ GPa. The critical load, $P_{\rm cr}$, for the dislocation nucleation is 18.4 N m^{-1}, corresponding to a hardness of 7.2 GPa. The hardness is obtained by dividing the critical load with the width of the indenter. The drop in the applied load due to the nucleation of dislocations is $\Delta P = 6.8\,{\rm N\,m^{-1}}$, similar to the value estimated by an elasticity model [8], which is $\Delta P = 7.7\,{\rm N\,m^{-1}}$. The P–d curves in general do not pass the origin due to the surface tension [8]. It should be pointed out since the present QCDFT is a static relaxation method, dislocations do not 'travel' from a location to another as in dynamical simulations; they are simply nucleated at a location where the energy is a minimum.

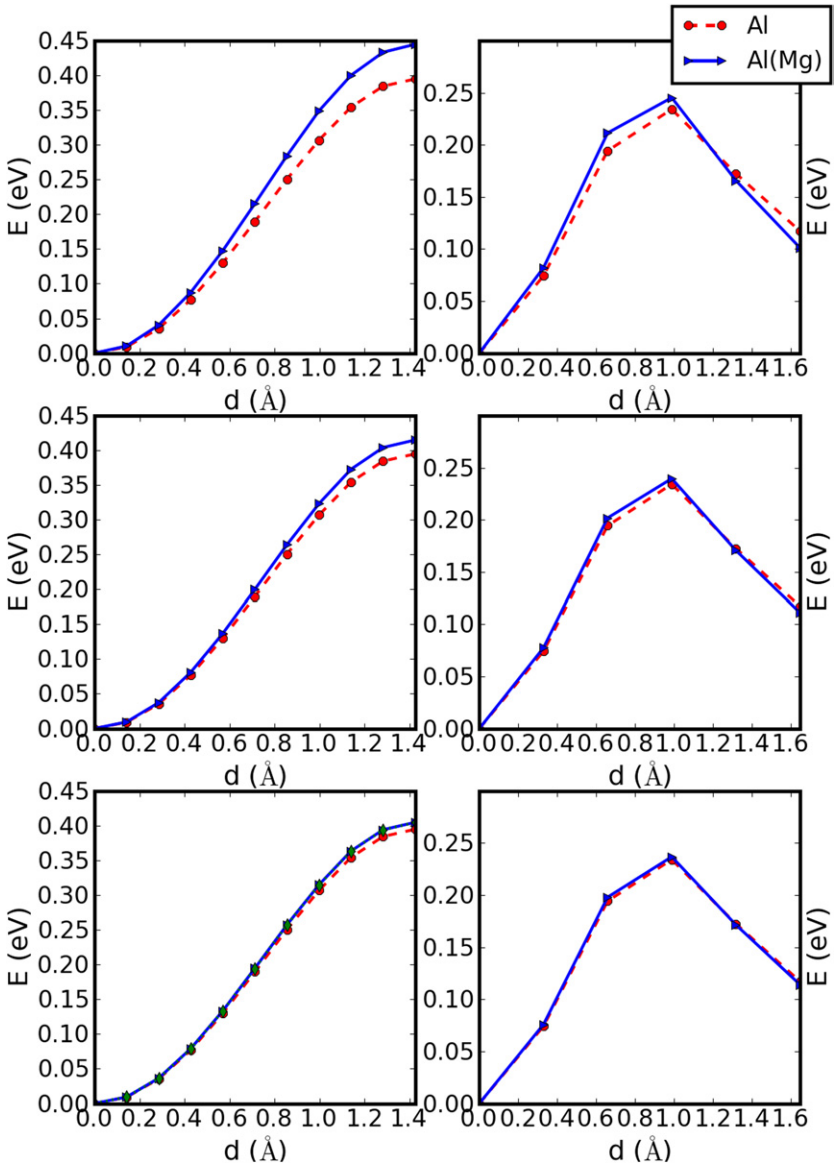

Figure 4. GSFEs as a function of Mg concentration and directions. The left (right) column represents the GSFE along the $[\bar{1}\,1\,0]$ ($[\bar{1}\,\bar{1}\,2]$) direction. The first, second and third rows present the GSFEs for Mg concentrations of 4.17%, 1.67% and 0.83%, respectively. The dashed (solid) line corresponds to the pure (alloy) systems. See text for details.

For randomly distributed impurities, the load–displacement curve shows a linear relation up to a depth of 8.0 Å, followed by a drop at $d = 8.1$ Å in figure 5. The slope of the initial linear part of the load–displacement curve is 26.7 GPa, rather close to the corresponding pure Al value. The maximum load in linear region is $P_{\rm cr}^{\rm im} = 19.2\,{\rm N\,m^{-1}}$, corresponding to a hardness of 7.5 GPa, which is 0.3 GPa or 4% greater than that of the pure Al. A pair of Shockley partial dislocations is nucleated at $x = -13$ Å, $y = -40$ Å and $x = 13$ Å, $y = -38$ Å, respectively, as shown in figure 6. The fact that the hardness of the Al–Mg alloy is greater

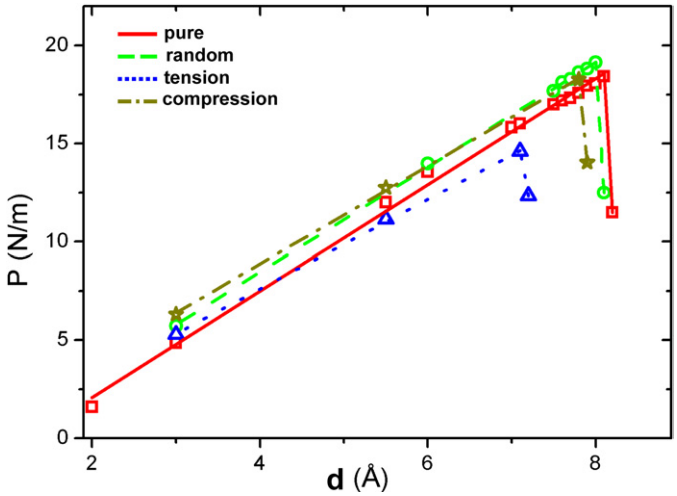

Figure 5. Load–displacement (P–d) plot for the nanoindentation of the Al thin film with a rigid rectangular indenter: *pure* (solid line), *random* (dashed line), *tension* (dotted line), *compression* (dashed–dotted line) obtained from QCDFT calculations. The lines are the best fit to the corresponding simulation data points.

than that of the pure Al is an indication of the strengthening effect of the Mg impurities on the ideal strength of Al. However, the magnitude of the strengthening is insignificant, and is on the order of the changes in the shear modulus. This finding is consistent with an experimental study on Cu–Ni solid solution alloys [40]; the nanoindentation measurements demonstrated the effect of solute impurities on the formation of dislocations in a previously dislocation-free region to be minimal. Moreover, the experimental study suggested that overall dislocation nucleation is strongly related to the shear modulus in this system. It is clear from our results that the origin of the strengthening is not due to the propagation of dislocations, but rather the nucleation of dislocations. The presence of randomly distributed Mg impurities hinders the nucleation of dislocations. In fact, only the leading partial dislocations are nucleated, trailing by stacking faults as shown in figure 6(*b*). This result is in contrast to the pure system where full dislocations are nucleated at a larger distance below the surface. The drop in the applied load due to incipient plasticity is $5.9\,\mathrm{N\,m^{-1}}$, less than that of the pure system ($6.8\,\mathrm{N\,m^{-1}}$). The smaller drop of the load in the random case is because partial dislocations are nucleated instead of full dislocations as in the pure system. We expect that the critical load/hardness corresponding to nucleation of full dislocations in this case will be higher because of work hardening (strengthening of a metal by plastic deformation).

The reason why partial dislocations are nucleated as opposed to full dislocations in the presence of random impurities can be understood from the following simple energetic consideration. E^{dis}, the energy of the dislocation can be approximated by the contributions of the elastic energy E^{el} and the stacking fault energy E^{sf}

$$\begin{aligned} E^{\mathrm{dis}} &= E^{\mathrm{el}} + E^{\mathrm{sf}} \\ &= \frac{\mu}{2\pi(1-\nu)} b^2 + \gamma_{\mathrm{isf}} * w, \end{aligned} \tag{7}$$

where μ, ν, b, γ_{isf} and w are the shear modulus, Poisson's ratio, the Burgers vector, the ISF energy and the width of the stacking fault, respectively. Here w is measured from the QCDFT

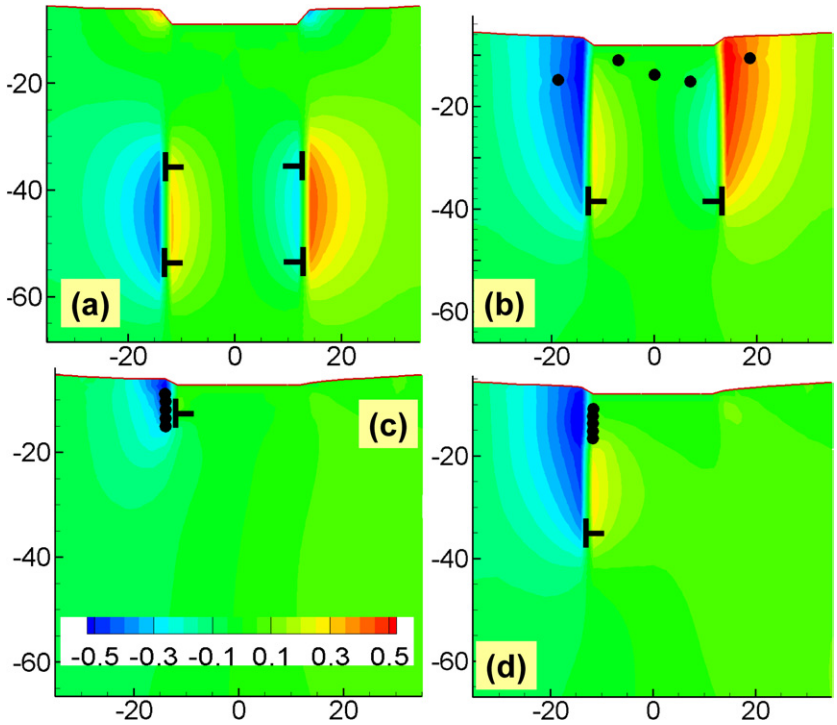

Figure 6. The out-of-plane displacement u_z corresponding to (*a*) *pure*, (*b*) *random*, (*c*) *tension*, (*d*) *compression* cases obtained from QCDFT calculations. The displacement ranges from −0.5 (blue) to 0.5 (red) Å. The black dots indicate the position of the Mg impurities. All distances are given in Å.

results. Because μ is increased in the presence of the impurities, the system could lower its energy by reducing b, i.e. dissociation into partials. Of course, it is energetically favorable only if $\gamma_{\rm isf}$ and w are not too large. The fact the $\gamma_{\rm isf}$ value is slightly reduced in the presence of Mg impurities helps the dissociation. Using the quantities tabulated in table 2, we find that the energy of the random impurities system (with two partial dislocations) relative to the perfect crystal is 0.91 eV lower than that of the pure system (two full dislocations). The Burgers vectors for full and partial dislocations are determined to be 2.85 Å and 1.65 Å, respectively. The width of the stacking fault (w) has two entries for the pure and random cases since two dislocations are nucleated.

For Mg impurities below the slip plane (the *tension* case), the load–displacement curve shows a linear relation up to a depth of 7.1 Å, followed by a drop at $d = 7.2$ Å (dotted line in figure 5). The maximum load in linear region is $P_{\rm cr}^{\rm im} = 17.8\,{\rm N\,m^{-1}}$, corresponding to a hardness of 6.5 GPa, which is 0.7 GPa or 10% smaller than the pure Al system. A single Shockley partial dislocation is nucleated at $x = -13$ Å, $y = -14$ Å as shown in figure 6(*c*). The drop in the applied load due to the dislocation nucleation is $2.3\,{\rm N\,m^{-1}}$.

Similarly, for Mg impurities above the slip plane (the *compression* case), the load–displacement curve is linear up to a depth of 7.8 Å, followed by a drop at $d = 7.9$ Å, as shown by the dotted-dashed line in figure 5. The maximum load in linear region is $P_{\rm cr}^{\rm im} = 18.3\,{\rm N\,m^{-1}}$, corresponding to a hardness of 7.1 GPa, which is 0.1 GPa smaller than the pure Al system. A single Shockley partial dislocation is nucleated at $x = -13$ Å, $y = -35$ Å in figure 6. The drop in the applied load due to the dislocation nucleation is $4.2\,{\rm N\,m^{-1}}$.

From the above results, we conclude that a linear distribution of Mg impurities can actually soften the material and render dislocation nucleation easier than in pure Al. In other words, the solid solution effect on dislocation nucleation depends sensitively on the local configuration of the impurities. In the three cases (of the same Mg concentration) studied here, the hardness of the alloys varies and the impurities can either increase or decrease the hardness, depending on their configuration. It should be emphasized that the change in hardness is associated with dislocation nucleation, not with dislocation propagation. Although it is well known that dislocation propagation (or dislocation-impurity interaction) depends sensitively on the impurity configuration, it is less recognized that the impurity configuration also affects dislocation nucleation.

The reason that the hardness in the tension case is less than that in the compression case can be understood from ionic size considerations. The ionic radius of Al is 0.54 Å, which is much smaller than that of Mg (0.86 Å). In the compression case, since smaller Al atoms are replaced by larger Mg atoms in a compression region, the substitution increases the compressive stress, and makes it more difficult to form edge dislocations, thus a higher hardness. On the other hand, the replacement of smaller Al atoms by larger Mg atoms in a tension region reduces the tension and makes it easier to form the dislocations, hence a lower hardness. Because the impurities in these cases are located on one side of the indentor, the symmetry is broken and a dislocation is nucleated only on one side of the thin film. Because only one partial dislocation is nucleated in the compression and tension cases, the energy of the two cases relative to the perfect crystal is much smaller, as shown table 2.

5. Conclusions

In summary, we use the recently introduced QCDFT method, which can simulate multi-million atoms based on DFT, to study solid solution effects on dislocation nucleation during nanoindentation. An Al thin film in the presence and absence of Mg impurities is examined. We predict that the solid solution effect depends sensitively on the local configuration of the impurities. Although a random distribution of the impurities increases the hardness of the material, linear distributions of impurities actually lower the hardness. In both cases, the effects are entirely due to dislocation nucleation; solid solution strengthening owing to dislocation motion is not considered here. Consistent with experimental results on Ni/Cu alloys, the change of the ideal strength is found to be small, of the same order of magnitude of the change in shear modulus. On the other hand, the incipient plasticity is observed to be quite different among the different distributions of impurities. In pure Al, two full dislocations are nucleated under the indentor with opposite sign. For a random distribution of impurities, two partial dislocations are nucleated instead. For linear distributions of the impurities, only one partial dislocation is nucleated. Our findings suggest that random distributions of Mg impurities offer the best means to harden Al.

Acknowledgments

The work at California State University Northridge was supported by NSF PREM grant DMR-0611562 and DoE SciDAC grant DE-FC02-06ER25791. The work at Princeton was supported by an NSF MRSEC and the Office of Naval Research (E.A.C.).

References

[1] Argon A S 2007 *Strengthening Mechanisms in Crystal Plasticity* (Oxford: Oxford University Press)
[2] Fischer-Cripps A C 2004 *Nanoindentation* (New York: Springer)

[3] Nix W D 1989 *Metall. Trans.* A **20** 2217
[4] Page T F, Oliver W C and Mchargue C J 1992 *J. Mater. Res.* **7** 450
[5] Oliver W and Pharr G 1992 *J. Mater. Res.* **7** 1564
[6] Gerberich W, Nelson J, Lilleodden E, Anderson P and Wyrobek J 1996 *Acta Mater.* **44** 3585
[7] Corcoran S G, Colton R J, Lilleodden E T and Gerberich W W 1997 *Phys. Rev.* B **55** R16057
[8] Tadmor E B, Miller R, Phillips R and Ortiz M 1999 *J. Mater. Res.* **14** 2233
[9] Gouldstone A, Koh H J, Zeng K Y, Giannakopoulos A E and Suresh S 2000 *Acta Mater.* **48** 2277
[10] Zhu T *et al* 2004 *J. Mech. Phys. Solids* **52** 691
[11] Hayes R L, Fago M, Ortiz M and Carter E A 2005 *Multiscale Modeling Simul.* **4** 359
Hayes R L, Fago M, Ortiz M and Carter E A 2008 *Multiscale Modeling Simul.* **7** 1003 (erratum)
[12] Hayes R L, Ho G, Ortiz M and Carter E A 2006 *Phil. Mag.* **86** 2343
[13] Gouldstone A *et al* 2007 *Acta Mater.* **55** 4015
[14] Hatch J E (ed) 1984 *Aluminum: Properties and Physical Metallurgy* (Materials Park, OH: American Society for Metals)
[15] Davis J (ed) 1993 *Aluminum and Aluminum Alloys* (Materials Park, OH: American Society for Metals)
[16] Zhang D and Picu R C 2004 *Modelling Simul. Mater. Sci. Eng.* **12** 121
[17] Han B Q and Lavernia E J 2005 *Adv. Eng. Mater.* **7** 457
[18] Cao B, Joshi S P and Ramesh K 2009 *Scr. Mater.* **60** 619
[19] Fago M, Hayes R L, Carter E A and Ortiz M 2004 *Phys. Rev.* B **70** 100102
[20] Peng Q, Zhang X, Hung L, Carter E A and Lu G 2008 *Phys. Rev.* B **78** 054118
[21] Tadmor E B, Ortiz M and Phillips R 1996 *Philo. Mag.* A **73** 1529
[22] Shenoy V B *et al* 1999 *J. Mech. Phys. Solids* **47** 611
[23] Choly N, Lu G, E W and Kaxiras E 2005 *Phys. Rev.* B **71** 094101
[24] Zhang X and Lu G 2007 *Phys. Rev.* B **76** 245111
[25] Zhang X, Wang C-Y and Lu G 2008 *Phys. Rev.* B **78** 235119
[26] Wang Y A and Carter E A 2000 *Theoretical Methods in Condensed Phase Chemistry* (Kluwer: Dordrecht) chapter 5
[27] Wang Y A, Govind N and Carter E A 1999 *Phys. Rev.* B **60** 16350
[28] Ercolessi F and Adams J B 1994 *Europhys. Lett.* **26** 583
[29] Knap J and Ortiz M 2003 *Phys. Rev. Lett.* **90** 226102
[30] Goodwin L, Needs R J and Heine V 1990 *J. Phys. Condens. Matter* **2** 351
[31] Huang C and Carter E A 2008 *Phys. Chem. Chem. Phys.* **10** 7109
[32] Perdew J P and Zunger A 1981 *Phys. Rev.* B **23** 5048
[33] Charpin T 2001 *A Package for Calculating Elastic Tensor of a Cubic Phases Using WIEN* (Paris: Laboratoire Des Gomatriaux de l'IPGP)
[34] Mehl M J, Osburn J E, Papaconstantopoulos D A and Klein B M 1990 *Phys. Rev.* B **41** 10311
[35] Tadmor E B, Miller R and Phillips R 1999 *J. Mater. Res.* **14** 2249
[36] Lu G, Kioussis N, Bulatov V V and Kaxiras E 2000 *Phys. Rev.* B **62** 3099
[37] Lu G, Orlikowski D, Park I, Politano O and Kaxiras E 2002 *Phys. Rev.* B **65** 064102
[38] Suresh S, Nieh T G and Choi B W 1999 *Scr. Mater.* **41** 951
[39] Shenoy V B, Phillips R and Tadmor E B 2000 *J. Mech. Phys. Solids* **48** 649
[40] Bahr D and Vasquez G 2005 *J. Mater. Res.* **20** 1947